



# Kent Academic Repository

**Sanderson, Taylor, Bradu, Adrian, Rajendram, Ranjan and Podoleanu, Adrian (2025) *Full-field optical coherence tomography system with a simplified dynamic focus mechanism*. Journal of Optics, 27 (11). ISSN 2040-8978.**

## Downloaded from

<https://kar.kent.ac.uk/112074/> The University of Kent's Academic Repository KAR

## The version of record is available from

<https://doi.org/doi:10.1088/2040-8986/ae19fb>

## This document version

Publisher pdf

## DOI for this version

## Licence for this version

CC BY (Attribution)

## Additional information

## Versions of research works

### Versions of Record

If this version is the version of record, it is the same as the published version available on the publisher's web site. Cite as the published version.

### Author Accepted Manuscripts

If this document is identified as the Author Accepted Manuscript it is the version after peer review but before type setting, copy editing or publisher branding. Cite as Surname, Initial. (Year) 'Title of article'. To be published in **Title of Journal**, Volume and issue numbers [peer-reviewed accepted version]. Available at: DOI or URL (Accessed: date).

## Enquiries

If you have questions about this document contact [ResearchSupport@kent.ac.uk](mailto:ResearchSupport@kent.ac.uk). Please include the URL of the record in KAR. If you believe that your, or a third party's rights have been compromised through this document please see our [Take Down policy](https://www.kent.ac.uk/guides/kar-the-kent-academic-repository#policies) (available from <https://www.kent.ac.uk/guides/kar-the-kent-academic-repository#policies>).

PAPER • OPEN ACCESS

# Full-field optical coherence tomography system with a simplified dynamic focus mechanism

To cite this article: Taylor Sanderson *et al* 2025 *J. Opt.* **27** 115301

View the [article online](#) for updates and enhancements.

## You may also like

- [Plastic ice in confined geometry: the evidence from neutron diffraction and NMR relaxation](#)  
J Beau W Webber, John C Dore, John H Strange et al.
- [Variability in IC5070: Two Young Stars with Deep Recurring Eclipses](#)  
Dirk Froebrich, Aleks Scholz, Justyn Campbell-White et al.
- [Computer Modelling Studies of Lithium Transport in Nanoporous and Bulk Beta-MnO<sub>2</sub>](#)  
Phuti Esrom Ngoepe, Thi X T Sayle and Dean C Sayle

# Full-field optical coherence tomography system with a simplified dynamic focus mechanism

Taylor Sanderson<sup>1,\*</sup> , Adrian Bradu<sup>1</sup> , Ranjan Rajendram<sup>2</sup>  and Adrian Podoleanu<sup>1</sup> 

<sup>1</sup> Applied Optics Group, University of Kent, CT2 7NH, Canterbury, United Kingdom

<sup>2</sup> Moorfields Eye Hospital and Institute of Ophthalmology, University College London, WC1E 6BT London, United Kingdom

E-mail: [tls23@kent.ac.uk](mailto:tls23@kent.ac.uk)

Received 5 June 2025, revised 21 October 2025

Accepted for publication 31 October 2025

Published 19 November 2025



## Abstract

Loss of focus in depth due to the mismatch between the coherence gate and the focus gate is a limiting factor in the achievable high lateral resolution in optical coherence tomography (OCT). This work adapts a simplified dynamic focus method, utilising only one mechanical element to a full-field OCT configuration, and demonstrates the capability to maintain the alignment of the coherence gate and the depth of the focus gates, at sample depths of up to 4 mm while using a high numerical aperture objective lens (NA = 0.5).

Keywords: optical coherence tomography, OCT, full-field OCT, dynamic focus, lateral resolution

## 1. Introduction

Optical coherence tomography (OCT) is a non-invasive, label-free imaging technique based on the principle of low coherence interferometry [1], capable of capturing volumetric images of a sample with micron-level axial resolution [2]. OCT has been widely adopted in biomedical applications with use in ophthalmology [3], endoscopy, optical biopsies and microscopy [4, 5].

Full-field OCT (FF-OCT) [6] is an implementation of OCT where the entire sample target area is illuminated. The scattered light is collected in parallel to produce a two-dimensional en-face image in a single frame using a 2D

detector such as a charge coupled device or a complimentary metal oxide semiconductor (CMOS) camera [7]. This approach forgoes the requirement of lateral scanners, as required in point-scanning OCT, enabling the possibility for FF-OCT instruments to be less costly than their flying spot counterparts. Time domain FF-OCT (TD-FF-OCT) allows a three-dimensional volume scan to be constructed by acquiring en-face images from different sample depths.

The lateral resolution,  $\delta x$ , can be estimated from the radius of the Airy disk,

$$\delta x = \frac{1.22 \lambda_0}{2NA} \quad (1)$$

where  $\lambda_0$  is the central wavelength of the spectrum emitted by the optical source and NA is the numerical aperture (NA) of the objective lens [8].

The depth of focus (DOF), alternatively labelled here as the focus gate, is defined by the confocal parameter,  $b$ , and is twice the Rayleigh range,

$$b = 2\Delta z_r = \frac{2\pi w_0^2}{\lambda_0}. \quad (2)$$

\* Author to whom any correspondence should be addressed.



Original Content from this work may be used under the terms of the [Creative Commons Attribution 4.0 licence](https://creativecommons.org/licenses/by/4.0/). Any further distribution of this work must maintain attribution to the author(s) and the title of the work, journal citation and DOI.

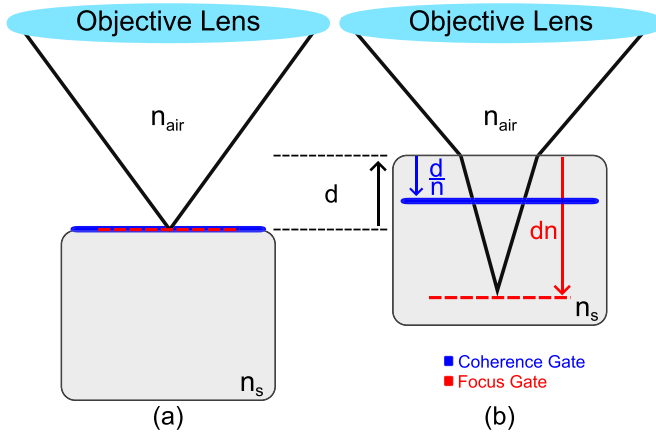


**Figure 1.** The relative positions of the focus gate and coherence gate. The blue line and dashed red line represent the respective positions of the focus and coherence gates. (a) shows the gates positioned, overlapping, on the sample surface. (b) shows the distances and direction moved of the gates, relative to the starting position in (a), when the sample is moved towards the objective lens by distance,  $d$ .

Taking the diffraction-limited beam waist as  $w_0 = \lambda_0 / \pi \text{NA}$ , the DOF can be defined as:

$$\text{DOF} = \frac{2n\lambda_0}{\text{NA}^2} \quad (3)$$

where  $n$  is the refractive index of the sample. It is apparent from equation (1) that the lateral resolution of an OCT system can be improved by increasing the NA of the objective lens. However, the use of a high NA objective lens greatly narrows the DOF. This presents a challenge for imaging at depth. When the coherence gate and focus gate are adjusted to overlap at the top of a sample (of a refractive index,  $n_s$ , different to that of the surrounding medium of air), and the sample is moved towards the OCT instrument, the coherence gate and focus gate positions move in opposite directions axially. This phenomenon is depicted in figure 1: when the sample is moved towards the objective lens by a distance,  $d$ , the focus shifts into the sample by  $dn_s$  while the coherence gate moves by  $d/n_s$ . The higher the NA of the lens, the narrower the DOF and the more pronounced the defocus effect. This occurs due to the coherence gate separating further from the focus gate.

TD OCT is compatible with dynamic focus. This consists of maintaining the overlap between the focus gate and the coherence gate while scanning the optical path length. Several techniques have been reported for dynamic focus [9, 10]. In general, dynamic focus employs at least two adjustable components within the OCT interferometer. In order to move the focus to different depths, the distance between the sample and the lens is varied, however, to synchronise the coherence gate with the new focus position, a second element is needed. This element, such as a translation stage, is used to adjust the optical path, in either the object or reference arm of the interferometer [11, 12].

In contrast, dynamic focus is not compatible with spectral domain (SD) OCT methods such as swept-source or

spectrometer-based OCT. In these methods, all depths along the axial range are interrogated at once, making dynamic focus techniques non-applicable. Instead, in SD-OCT, numerical refocusing techniques can be applied in post-processing to correct for focus and coherence gate separation. This processing can effectively extend the DOF without requiring any additional components in the imaging system [13]. In general, these methods use the phase information from out-of-focus signals to apply a numerical correction to the aberrated wavefront and recover a focused image. In SD-OCT, this approach has been shown to extend the axial imaging range by several times the DOF [13]. However, in instances where a high NA is required ( $\text{NA} > 0.1$ ), the narrow DOF reduces its effectiveness. There have been reports of numerical refocusing in TD-OCT with immersion objectives, however the same DOF linked limitation still applies [14]. Typically, numerical refocusing methods are limited to inhomogeneous samples of the known refractive index, with exceptions being computationally intensive, requiring high-performance hardware [13].

An elegant approach to the dynamic focus procedure was introduced in [15], where through a single mechanical movement, both coherence and focus gates are moved in synchrony. This approach combines the sample and reference arms on a single translation stage, with the light in the reference arm back reflected, doubling the path length change as the objective lens is scanned towards the sample. This compensates for the defocus in samples of refractive index  $n = \sqrt{2}$ , a value close to the index of refraction of most biological tissues [16]. However, the need to route the light in both the sample and reference arms on a single translation stage adds significant complexity to the system layout.

An improved dynamic focus optics configuration was introduced in [17], where again, a single translation stage is employed; however, with a much simplified architecture, where the change in path length is executed in the sample arm only. In other words, such a method mechanically decouples the reference and sample arm changes. Not having to route the light in the reference arm via the translation stage gives more room to the optics assembly. This makes it possible to adapt such a configuration to an FF setup.

This layout achieves the same result of synchronising the movement of the coherence gate and focal gate for a sample of  $n = \sqrt{2}$ , however, integrating this mechanism into an FF instrument introduces additional optical and mechanical constraints, which are addressed in the following sections. The potential for such an approach to be paired with accessible hardware is also considered by employing a single-board computer (Raspberry Pi) and an inexpensive 2D CMOS camera sensor.

## 2. Methods

Figure 2 presents a schematic diagram of the system, which is based on a Linnik interferometer configuration. The optical source is a Superlum Broadlighter 890 (D890 HP) super luminescent diode (SLD), with a central wavelength of

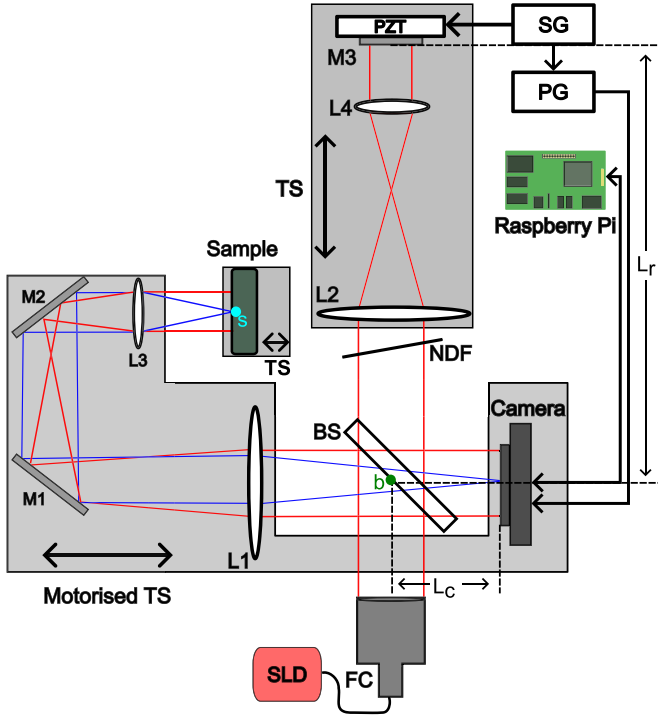


**Figure 2.** Schematic diagram of the dynamic focus FF-OCT system. SLD: super luminescent diode, FC: fibre collimator, L1, L2:  $f = 150$  mm achromatic lenses (Thorlabs AC-254-150-B), L3, L4:  $f = 8.0$  mm 20x aspheric objectives (Newfocus 5724-B-H, NA = 0.5), BS: 50:50 plate beam splitter, TS: translation stage, M1, M2: gold mirrors, M3: reference mirror, NDF: variable neutral density filter, PZT: Piezoelectric Transducer, SG: signal generator, PG: pulse generator.

$\lambda_0 = 890$  nm and a spectral bandwidth of  $\Delta\lambda = 150$  nm. Assuming a Gaussian spectral profile, a theoretical OCT axial resolution of  $\delta z = 2.33$   $\mu$ m is estimated.

Collimated light from the SLD enters the system where it is divided by the beamsplitter (BS) into a reference and a sample arm. In the sample arm, a telescope is formed using lenses L1 and L3, achieving magnification  $M = 18.75$ . Considering the size of the camera sensor area used, this results in a field of view of  $270 \times 200$   $\mu$ m<sup>2</sup>.

The inexpensive camera (FLIR Blackfly S BFS-U3-16S2M-BD) has a sensor of  $1440 \times 1080$  square pixels of  $3.45$   $\mu$ m with 12-bit depth. To control the camera and generate the OCT images, the camera is paired with a Raspberry Pi 5 single board computer, where raw sensor data can be stored directly in the device's random access memory (RAM), before also being processed on the device.

In the reference arm, a telescope identical to the one in the sample arm is formed, using lenses L2 and L4, to compensate for the dispersion mismatch between the interferometer arms. The reference mirror, M3, is mounted on a piezoelectric transducer (PZT) to introduce a controlled phase shift between captured frames so that an OCT image can be extracted from a few carefully captured interferograms, using phase shifting interferometry.

The configuration in figure 2 routes only the light in the object arm via the translation stage, and by moving it, both

gates are scanned axially in synchrony in a sample of  $n \approx 1.41$ , in a similar manner to [17]. However, the implementation of this method from a point-scanning to an FF setup requires additional considerations in the system design. In [17], fibre optics were used between the elements on the translation stage and the photodetector so imaging was simple, from a single point in the sample to a single point on the photodetector, via a single mode fibre. In FF imaging, a telescope is used in figure 2 to relay each point in the sample to its corresponding pixel on the detector, which is located in a conjugate image plane. In FF-OCT, the conjugate image planes of the sample and reference arms must be precisely aligned to ensure that each camera pixel corresponds to the same spatial point in both optical paths, as misalignment can result in a reduced interference contrast and a degradation of the signal to noise ratio [18].

As this dynamic focus method requires the physical movement of the sample arm, all optical components, including the camera, are mounted together on the motorised translation stage to maintain alignment and magnification when the dynamic focus mechanism is engaged. For ease of reference arm length adjustment, the telescope formed by L2 and L4 must also be mounted on its own translation stage. In contrast to simpler single detector arrangements in point-scanning, OCT and FF-OCT require more complex detection methods such as phase-shifting interferometry, which can make FF-OCT more sensitive to phase errors [19]. Stable phase modulation and acquisition are therefore essential, which is facilitated here by a camera with a global shutter.

The requirement of the camera to also be displaced by the sample arm when scanning the object alters the consideration of the path length changes compared to the point scanning implementation [17]. Referring to the system diagram in figure 2, the key optical path lengths are defined as follows from the detection plane:

- Reference arm length:  $L_r$
- Distance from BS to camera:  $L_c$
- Sample arm length between points  $s$  (a point on the sample surface) and  $b$  (centre of BS):  $L_{sb}$

When the focus and coherence gates are positioned together at the closest surface of the sample to the objective lens, L3, as would be the case at the start of imaging, the optical path difference (OPD) between the two interferometer arms at the camera is equal, as follows:

$$2L_{sb} + L_c = 2L_r + L_c. \quad (4)$$

If the dynamic focus is engaged and the sample arm translation stage is shifted towards the sample by a distance  $x$ ,  $L_c$  increases by  $x$  in the reference arm. In the sample arm  $L_c$  also increases by  $x$ , while  $L_{sb}$  decreases by  $2x$  and the new focus position in the sample shifts to point inside the sample that corresponds to a round trip increase in the OPD of  $2n^2x$ . To keep the focus and coherence gate together at this new depth, equation (4) becomes:

$$2(L_{sb} - 2x) + 2n^2x + L_c + x = 2L_r + L_c + x. \quad (5)$$

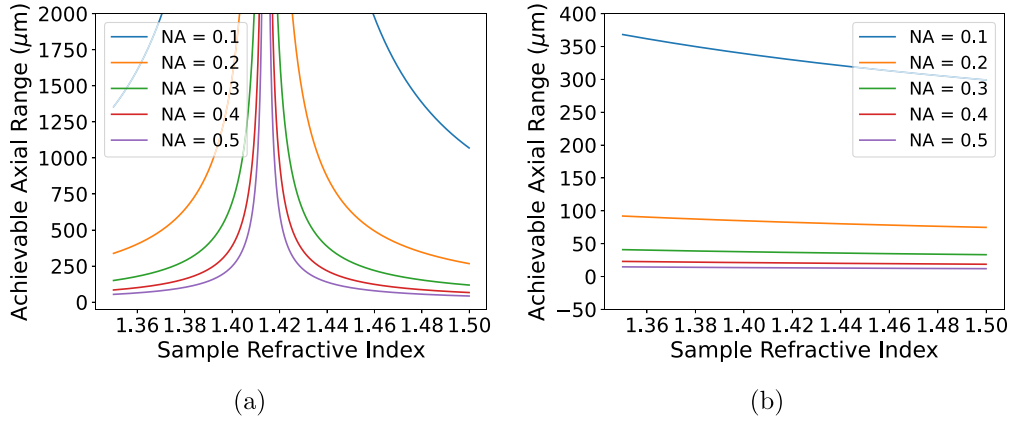


**Figure 3.** Achievable axial range for different values of sample refractive index and objective lens NA.

Solving for  $n$  gives  $n = \sqrt{2}$ , which confirms that the functionality of the original point-scanning dynamic focus method is preserved in this FF implementation.

For the mismatch between the coherence gate and the focus gate in depth ( $\Delta$ ) to be minimised, the refractive index of the sample must be approximately equal to  $\sqrt{2}$ . This value is consistent with the refractive index of most biological samples ( $\approx 1.34 - 1.65$ ) [16] where soft tissues such as skin have refractive indices ranging between 1.34 – 1.56 and the human eye between 1.36 – 1.45. Thus, some of the most imaged biomedical samples lie within the ideal range of refractive index for this method. This is particularly relevant when considering that an image of sufficient quality can be obtained without perfect alignment of the focus and coherence gates, providing the coherence gate position is within half of the DOF. The achievable axial range for a given sample refractive index and objective lens NA can be described by equation (6),

$$d < \left| \frac{\lambda_0 n}{NA^2 (n^2 - 2)} \right|. \quad (6)$$

Figure 3(a) presents the achievable axial range at which a good quality image can theoretically be obtained using the dynamic focus system, where the coherence gate is within the focus extension (half the DOF), as a function of deviations of the index of refraction from the ideal value versus the NA of the lens L3. In figure 3(b) the depth at which the coherence gate remains within the focus extension is shown for a system without dynamic focus with the sample being moved towards the objective lens.

A significant improvement in the achievable axial range is observed over the range of NA (0.1 - 0.5), particularly around the optimum sample refractive index  $n \approx 1.41$ . Even with a significant deviation from the optimum, the system retains a better focus in depth even with a high NA of 0.5.

The PZT is driven by a 25 Hz sinusoidal waveform generated by a signal generator (SG). A pulse generator (PG) is used to supply the camera's hardware trigger with a 100 Hz transistor–transistor logic signal. Each pulse triggers the camera to capture an interferogram and buffer it into RAM.

The waveforms from the signal and pulse generators are synchronised with an adjustable phase in order to control the optimal trigger for each capture. The dependence of the interference signal with time, due to the phase modulation, depends on the phase,  $\theta$ , as detailed below: [20]

$$I(x, y, t) = I(x, y) + A(x, y) \cos[\phi(x, y) + \psi \sin(\omega t + \theta)] \quad (7)$$

where  $I$  is the intensity of the DC terms,  $A$  is the interference amplitude,  $\phi$  is the optical phase and  $\psi$  the amplitude of the phase modulation.

By taking linear combinations of raw interferograms, the amplitude and phase of the interferogram can be extracted while rejecting the incoherent background light present on the sensor. This is achieved using a four phase shifting interferometry method, where combinations of four 2D interferograms were calculated as follows [21],

$$E_\alpha = F_1 - F_2 + F_3 - F_4 \quad (8)$$

$$E_\beta = F_1 - F_2 - F_3 + F_4. \quad (9)$$

So the amplitude of the interference signal can then be defined as follows,

$$A(x, y) = (E_\alpha^2 + E_\beta^2)^{1/2} \quad (10)$$

where  $F_1$  to  $F_4$  are frames captured with a phase difference of  $\pi / 2$  between each frame.

Sample imaging is performed as outlined below:

- The sample arm stage is scanned sequentially towards the sample in steps corresponding to the axial resolution.
- Four phase-shifted interferograms are captured at each sample depth.
- The interference amplitude is computed using equation (10).
- When the desired sample depth is reached, the amplitude is saved as a volumetric image.



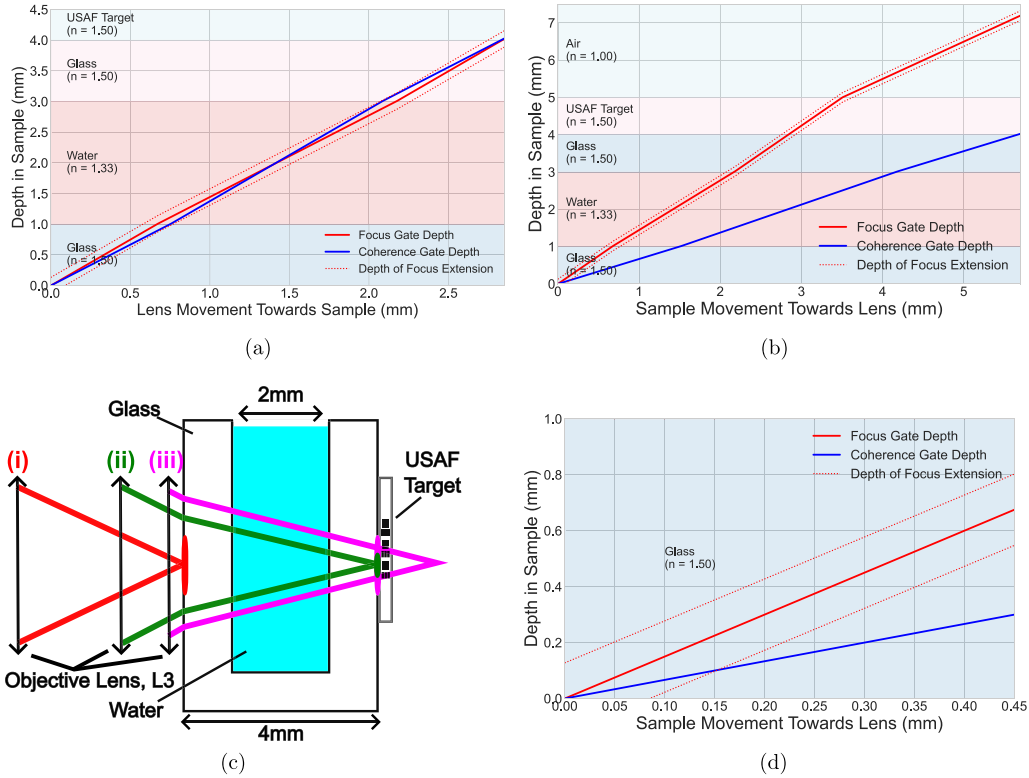


**Figure 4.** Theoretical depictions of the separation of the focus and coherence gates within the sample of large axial extension, 4 mm. An  $NA = 0.1$  is used here so that the DOF is visible on this scale. (a) Dynamic focus, i.e scanning the sample arm translation stage. (b) The sample being moved towards the objective lens L3, with the sample arm at rest. (c) Diagram of the cuvette + USAF sample used for this demonstration of dynamic focus. (d) A zoomed plot of (b) to demonstrate where the separation of the coherence gate from the focus occurs without use of the dynamic focus mechanism.

### 3. Results and discussion

To aid in the interpretation of the experimental results, theoretical depictions of the relative positions of the focus and coherence gates within the sample are presented in figures 4(a) and (b) for the dynamic focus and non-dynamic focus cases, respectively. In the case of non-dynamic focus, the sample itself is moved towards the objective lens, while the translation stage is held at rest.

The sample used for this demonstration is shown in figure 4(c) and consists of a glass cuvette ( $n \approx 1.50$ ) filled with water ( $n = 1.33$ ). This approximates the combined refractive index over the whole axial extension of the test object (4 mm) of  $n_{\text{combined}} \approx 1.415$ , which is close to the optimum value of the sample refractive index for this system. A USAF 1951 resolution test target was placed on the far side of the cuvette to test the focus and sharpness of the OCT image after scanning the sample with both methods. Figure 4(c), (i) depicts the starting position of the objective lens, focus and coherence gates, (ii) shows the change in positions when using the dynamic focus, (iii) shows the relative positions when the sample is moved towards the objective lens.

From Figure 4(a) it is evident that although the focus and coherence gates do have some separation within the

sample, as the focus is shifted through the sample layers, this is within the DOF. In addition, by the time the focus reaches the position of the USAF target on the back of the cuvette, the two gates overlap again. From this, theoretically an image that is in focus can be obtained at an axial displacement of 4 mm into the sample from the starting point on the surface. This range exceeds the DOF of the lens used more than ten times. This is in contrast to 4(b), where the coherence gate rapidly separates from the DOF extension after a sample depth of 0.10 mm, presented in the zoomed figure 4(d).

A comparison of the en-face OCT images is shown in figure 5, obtained from the cuvette sample described in figure 4. Figure 5(a) shows the resulting USAF image when using dynamic focus, shifting the sample arm translation stage towards the cuvette, while (c) shows the same area of the target but imaged after the sample is displaced towards the objective lens.

It is evident in figure 5 that the image obtained using the dynamic focus method, 5(a), is sharper and better focused than the image obtained without the dynamic focus, 5(c), a result consistent with the plots presented in figure 4. To document this improvement, edge response functions (ERFs) of the two images, 5(b) and 5(d), for the same area of the USAF

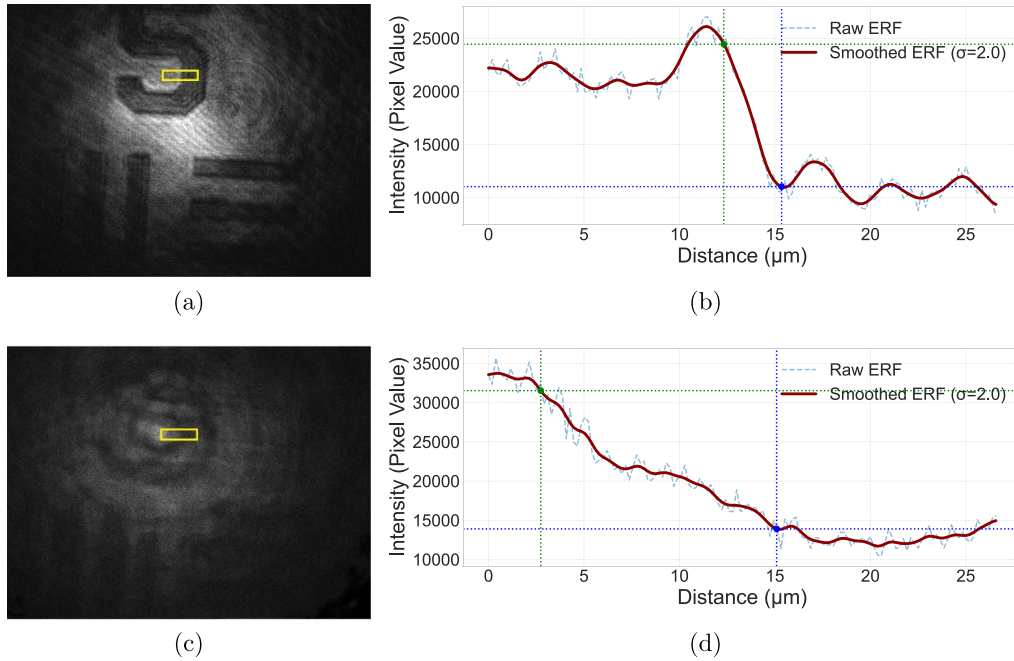


**Figure 5.** En-face OCT images of the USAF target on the sample depicted in figure 4(c), using a 0.5 NA objective lens, demonstrating a comparison of the dynamic focus method and shifting the focus by moving the sample. (a) Image of the USAF target using dynamic focus, showing group 5 element 1. (b) Edge response function of the marked area of the number corresponding to group 5 (a). (c) The same area of target as in (a) but imaged after the sample was moved towards the objective lens. (d) Edge response function of the marked area in (b).

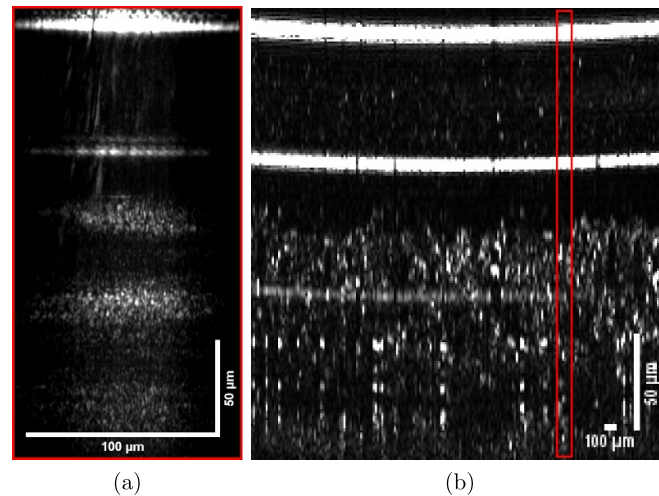


**Figure 6.** B-scans of an infrared detection card. (a) Imaged with the time domain full-field dynamic focus system presented in this paper. (b) A comparison image, obtained with a flying spot, swept-source OCT system at 1060 nm with  $NA \approx 0.1$ . The red rectangle highlights the much smaller lateral size of the image depicted in (a).

target are evaluated. The measured ERFs were smoothed with a Gaussian filter ( $\sigma = 2$  pixels) to reduce high frequency noise, and the 10%–90% rise distances were extracted. The measured 10%–90% rise distances were  $3.03 \mu\text{m}$  and  $12.35 \mu\text{m}$  for the dynamic focus image and non-dynamic focus images, respectively, confirming the significant focus improvement that can be achieved by this method.

For figure 5(a) the focus and coherence gate separation was estimated to be  $4.45 \mu\text{m}$  at the USAF target inside the sample. This separation remains within half of the DOF,  $5.34 \mu\text{m}$ .

Comparatively, without dynamic focus in figure 5, the separation of the gates in the sample is  $2.00 \text{ mm}$ , well exceeding the DOF.

The FF system was also tested for its ability to produce a cross-sectional image (B-scan) of an infrared card, as shown in figure 6(a). The card consists of a succession of layers, two transparent plastic laminate layers followed by a more scattering sample than was used for figure 5, the phosphor layer. A comparison image, figure 6(b), of the same infrared card is shown, obtained with a point-scanning swept-source OCT



system with an objective lens of small NA of 0.1 and centre wavelength of 1060 nm.

Comparing the two images, both the top and bottom layers of the laminate in addition to the phosphor layer can be distinguished in the B-scans. However, due to the high spatial coherence of the SLD source used, the coherence gate is affected by the multiple scattering from the sample. This leads to some degradation in image quality, likely from speckle noise and crosstalk between lateral pixels in the camera sensor [22, 23]. This is particularly noticeable in the more scattering phosphor layer but can also be seen in the lower intensity of the second laminate layer when compared to the swept-source image 6(b).

#### 4. Conclusion

The adaptation of the dynamic focus method in [17] to FF OCT has demonstrated effective performance in maintaining the focus and coherence gate alignment when using a high NA objective lens ( $NA = 0.5$ ). This is verified experimentally and consistent with the theoretical model presented. En-face and cross-section OCT images were produced, demonstrating their potential applicability to soft tissue imaging. Noise arising from multiple scattering, including speckle and lateral pixel crosstalk is particularly apparent in figure 6 for a scattering sample. To minimise these effects, future work could explore reducing the spatial coherence of the light source using diffusive elements such as lengths of multimode fibre [24, 25] or replacing the optical source with a thermal emitter [12, 26], both well-established approaches in FF OCT.

Compared to dual translation stage approaches for dynamic focus in FF-OCT, this single stage approach can achieve comparable functionality with a simpler mechanical arrangement. It also does not require prior knowledge of the refractive index of the sample to synchronise the gates. However, this method is designed to operate around a refractive index of  $n \approx 1.41$  for optimal synchronisation of the focus and coherence gates. If the sample refractive index deviates significantly from this optimal value, the achievable axial range is reduced. However, a consideration of the relationship between the lateral resolution and achievable axial range can be made to optimise the method, depending on the desired application (figure 3(a)).

In practice, this trade-off is unlikely to pose a major limitation for imaging biological samples, as the optimal refractive index lies centrally in the range of most biological samples. On the other hand, numerical refocusing approaches can digitally adjust the focus in post-processing to extend the useful axial imaging range, without requiring mechanical motion. However, the performance of numerical refocusing techniques is limited to only several times the DOF, after which the retrievable signal diminishes and the reconstructed image quality degrades [13]. Numerical methods that do not require prior knowledge of the sample's refractive index are typically the most computationally intensive, with applicability currently limited to state-of-the-art systems. In contrast, the setup

presented here demonstrates a dynamic focus approach in a mechanically simple and hardware accessible form.

Although the method detailed in this manuscript is limited by the relationship between NA and the sample's refractive index, it remains effective within those constraints. When combined with a numerical refocusing approach that is compatible with inhomogeneous samples of unknown refractive index, the two methods can be complementary. This combination could potentially enable high NA imaging of samples whose refractive indices deviate significantly from the optimal value, over an extended axial range, which would not be achieved with either method in isolation.

#### Data availability statement

All data that support the findings of this study are included within the article (and any supplementary files).





#### Acknowledgments

TS acknowledges support from the University of Kent Global Challenges Doctoral Centre and thanks Manuel Marques for providing the swept-source comparison image in figure 6(b). AB acknowledges the support of the Royal Society, Project PARSOCT, RGS/R1/221324 and the support of the Academy of Medical Sciences/the Wellcome Trust/the Government Department of Business, Energy and Industrial Strategy/the British Heart Foundation/Diabetes UK Springboard Award SBF007100162. AP acknowledges the NIHR BRC4-05-RB413-302, Imaging, Visual Assessment & Digital Innovation, at Moorfields Eye Hospital NHS FT and UCL Institute of Ophthalmology, the BBSRC 5DHiResE BB/S016643/1 and BB/X003744/1, the DPFS MRC 662915 to UoNottingham and UoKent, the EPSRC, FoVenOCT, EP/X000125/1, the National Institute for Health Research, i4i; NIHR202879 and the University of Kent's Biotechnology and BBSRC funded Impact Acceleration Account, BBSRC BB/X511158/1 and (MRC) funded Impact Acceleration Account, MR/X502753/1.

#### Conflict of interest

Adrian Podoleanu is a co-inventor of patents for the University of Kent.

#### ORCID iDs

Taylor Sanderson  0009-0004-2483-4357  
 Adrian Bradu  0000-0002-6890-1599  
 Ranjan Rajendram  0000-0003-3926-8824  
 Adrian Podoleanu  0000-0002-4899-9656

## References

- [1] Huang D *et al* 1991 Optical coherence tomography *Science* **254** 1178–81
- [2] Aumann S, Donner S, Fischer J and Müller F 2019 Optical Coherence Tomography (OCT): Principle and Technical Realization *High Resolution Imaging in Microscopy and Ophthalmology: New Frontiers in Biomedical Optics* ed J F Bille (Springer) pp 59–85
- [3] Drexler W and Fujimoto J 2008 State-of-the-art retinal optical coherence tomography *Prog. Retin. Eye Res.* **27** 45–88
- [4] Gora M J, Suter M J, Tearney G J and Li X 2017 Endoscopic optical coherence tomography: technologies and clinical applications [invited] *Biomed. Opt. Express* **8** 2405
- [5] Brezinski M E, Tearney G J, Bouma B E, Izatt J A, Hee M R, Swanson E A, Southern J F and Fujimoto J G 1996 Optical coherence tomography for optical biopsy: properties and demonstration of vascular pathology *Circulation* **93** 1206–13
- [6] Dubois A, Vabre L, Boccara A-C and Beaurepaire E 2002 High-resolution full-field optical coherence tomography with a Linnik microscope *Appl. Opt.* **41** 805–12
- [7] Wang L, Fu R, Xu C and Xu. M 2022 Methods and applications of full-field optical coherence tomography: a review *J. Biomed. Opt.* **27** 050901
- [8] Tomlins P H and Wang R K 2005 Theory, developments and applications of optical coherence tomography *J. Phys. D: Appl. Phys.* **38** 2519–35
- [9] Dubois A 2017 Focus defect and dispersion mismatch in full-field optical coherence microscopy *Appl. Opt.* **56** 150
- [10] Qi B, Phillip Himmer A, Gordon L M, Yang X D V, Dickensheets L D and Vitkin I A 2004 Dynamic focus control in high-speed optical coherence tomography based on a microelectromechanical mirror *Opt. Commun.* **232** 123–8
- [11] Pircher M, Götzinger E and Hitzenberger C K 2006 Dynamic focus in optical coherence tomography for retinal imaging *J. Biomed. Opt.* **11** 054013
- [12] Dubois A, Moneron G and Boccara C 2006 Thermal-light full-field optical coherence tomography in the 1.2  $\mu\text{m}$  wavelength region *Opt. Commun.* **266** 738–43
- [13] Kumar A, Drexler W and Leitgeb R A 2014 Numerical focusing methods for full field OCT: a comparison based on a common signal model *Opt. Express* **22** 16061
- [14] Min G, Kim J W, Choi W J and Lee B H 2012 Numerical correction of distorted images in full-field optical coherence tomography *Meas. Sci. Technol.* **23** 035403
- [15] Schmitt J M, Lee S L and Yung K M 1997 An optical coherence microscope with enhanced resolving power in thick tissue *Opt. Commun.* **142** 203–7
- [16] Khan R, Gul B, Khan S, Nisar H and Ahmad I 2021 Refractive index of biological tissues: review, measurement techniques and applications *Photodiagnosis Photodyn. Ther.* **33** 102192
- [17] Hughes M, Podoleanu AGH 2009 Simplified dynamic focus method for time domain OCT *Electron. Lett.* **45** 623
- [18] Blavier M, Glanc M and Rousset G 2021 Analysis of the impact of optical aberrations in en-face full-field OCT microscopy *Opt. Express* **29** 2204
- [19] Zhu Y and Tian A 2024 Influence of phase-shifting error of phase-shifting interferometry on the phase accuracy recovery *J. Opt.* **53** 363–82
- [20] Dubois A 2001 Phase-map measurements by interferometry with sinusoidal phase modulation and four integrating buckets *J. Opt. Soc. Am. A* **18** 1972
- [21] Sasaki O, Okazaki H and Sakai M 1987 Sinusoidal phase modulating interferometer using the integrating-bucket method *Appl. Opt.* **26** 1089
- [22] Liba O, Lew M D, SoRelle E D, Dutta R, Sen D, Moshfeghi D M, Chu S and Zerda A D L 2017 Speckle-modulating optical coherence tomography in living mice and humans *Nat. Commun.* **8** 15845
- [23] Auksoorius E, Borycki D and Wojtkowski M 2019 Crosstalk-free volumetric *in vivo* imaging of a human retina with Fourier-domain full-field optical coherence tomography *Biomed. Opt. Express* **10** 6390
- [24] Auksoorius E, Borycki D, Wegrzyn P, Žičkienė I, čius K A, Sikorski B L and Wojtkowski M 2022 Multimode fiber as a tool to reduce cross talk in Fourier-domain full-field optical coherence tomography *Opt. Lett.* **47** 838
- [25] Dhalla A-H, Migacz J V and Izatt J A 2010 Crosstalk rejection in parallel optical coherence tomography using spatially incoherent illumination with partially coherent sources *Opt. Lett.* **35** 2305
- [26] Laude B, De Martino A, Drévilion B, Benattar L and Schwartz L 2002 Full-field optical coherence tomography with thermal light *Appl. Opt.* **41** 6637